Structural periodicity dependent scattering behavior in parity-time symmetric elastic metamaterials

Jianlin Yi,[1,2] Zhaoyang Ma,[3] Rongyu Xia,[1] Mehrdad Negahban,[4] Changqing Chen,[2] and Zheng Li[1,*]

[1]*State Key Laboratory for Turbulence and Complex Systems, College of Engineering, Peking University, Beijing 100871, China*

[2]*Department of Engineering Mechanics, CNMM and AML, Tsinghua University, Beijing 100084, China*

[3]*School of Mechanics and Engineering Science, Shanghai University, Shanghai 200444, China*

[4]*Mechanical & Materials Engineering, University of Nebraska-Lincoln, Lincoln, Nebraska 68588, USA*

(Received 13 March 2022; revised 10 June 2022; accepted 27 June 2022; published 8 July 2022)

We investigate the effect of structural periodicity on elastic longitudinal and flexural wave propagation in parity-time ($\mathcal{PT}$) symmetric prototypical elastic metamaterial rods and beams. Through theoretical analysis and numerical demonstration, we reveal the link between the observed band structure of infinite periodic $\mathcal{PT}$ symmetric elastic metamaterials and the unique scattering properties of the corresponding finite periodic $\mathcal{PT}$ symmetric systems. In particular, we study the coherent perfect absorber and laser (CPAL). There is an observed periodic-like occurrence of the CPAL formation when varying the cell number in the finite periodic metamaterial that correlates to the band structure of the infinite periodic system. For this, we provide simple equations to estimate the periodicity and the minimum cell number. Using a piezoelectric-aided elastic metamaterial consisting of piezoelectric patches and active circuits, we propose a feasible configuration to realize tunable flexural wave CPALs in a periodic-structured $\mathcal{PT}$ symmetric metamaterial beam, and demonstrate that the CPAL can be induced in the Bragg's bandgap.

DOI: 10.1103/PhysRevB.106.014303

I. INTRODUCTION

Effective control of elastic wave propagation is a long-lasting topic that has been studied for many decades and has vital significance in nondestructive testing, medicine, and signal processing. Man-made structures, such as phononic crystals and metamaterials, have recently produced new strategies to control the propagation of elastic waves [1,2]. These artificial structures show many interesting characteristics. They can, for example, realize negative refraction [3], focusing [3–5], cloaking [6], nonreciprocal transmission [7], and asymmetric response [8–10]. These all result from designed macroscopic and/or phase properties such as effective negative mass and stiffness of the structure [11]. However, these effects have mainly been carried out by means of the modulation of the real part of the elastic or other material parameters. More recently, the emergent concept of parity-time ($\mathcal{PT}$) symmetry and, more generally, non-Hermitian physics, has enabled wave control in the complex domain [12] and has opened a new field for the manipulation of wave propagation.

Non-Hermitian systems are open systems with loss and/or gain. The study of non-Hermitian physics [13,14] was stimulated by the breakthrough discovery that the spectra of complex Hamiltonians, which are $\mathcal{PT}$ symmetric can also be real and positive [15]. Because of their concise form and unique properties, $\mathcal{PT}$ symmetric systems, as one of the most important subsets of non-Hermitian systems, have been explored in optics [16,17], acoustics [18,19], mechanics [20,21], magnetics [22], electronics [23], and atomic gases [24]. A result of this has been the observation/realization of many unconventional behaviors, such as spectral singularities [25], coherent perfect absorber and laser (CPAL) [26], unidirectional invisibility or unidirectional zero reflection [27,28], nonreciprocal transmission [29,30]. Although $\mathcal{PT}$ symmetric systems have been extensively explored in many branches of physics, and there has been considerable achievements, especially in optics [31,32], relatively speaking, the study of wave propagation in $\mathcal{PT}$ symmetric elastic solid systems remain very limited [20,21,30,33–36].

The introduction of $\mathcal{PT}$ symmetry in the elastic domain will not only extend elastic wave theory, but also provide new strategies to design high-performance elastic wave devices. For example, the linear sensitivity observed using traditional methods for damage detection in nondestructive testing has been enhanced through exploiting wave propagation in $\mathcal{PT}$ symmetric elastic systems [35]. Furthermore, nonreciprocal microwave surface elastic wave device design using $\mathcal{PT}$ symmetric resonators has been reported [30], and other efforts have also been made in exploring the properties of $\mathcal{PT}$ symmetric elastic systems [20,21,33,34,37]. However, much of this work has only considered wave propagation in $\mathcal{PT}$ symmetric elastic systems consisting of one or several pairs of loss and gain, and with only few studies focused on periodic $\mathcal{PT}$ symmetric systems. So far, the periodic effects remain elusive. The CPAL, as lasing or antilasing, is well known in $\mathcal{PT}$ symmetric optical and electromagnetic systems [26,38–40] and allows the system to behave simultaneously as a laser or an absorber depending on the characteristics of the incident waves. It has been reported that the scattering

*lizheng@pku.edu.cn

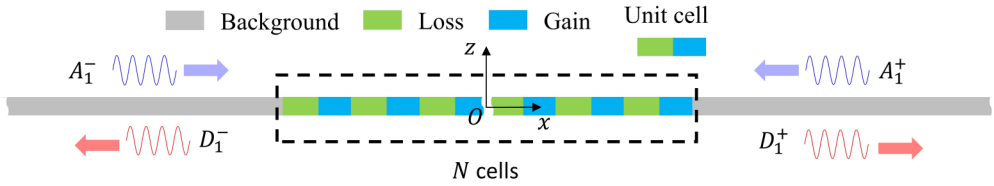

FIG. 1. The N-cell periodic $\mathcal{PT}$ symmetric metamaterial bar. The global coordinate Oxz is located at the center, and the x-z plane shows the side view of the rod with x along the axial direction.

properties of $\mathcal{PT}$ symmetric systems are cell-number-dependent, and the CPAL can be approached by tuning the number of cells [19,37,41]. We show the link between the CPAL and the band structure of infinite periodic $\mathcal{PT}$ symmetric systems, showing that the frequency, the minimum cell number, and the periodicity of the CPAL are related to the Bloch wavenumber.

Developing a CPAL for elastic waves could have significant impact. However, realization of a CPAL requires overcoming the intrinsic difference in the physical equations between optics, airborne acoustics, and elastic mechanics, and finding methods for obtaining gain. Generally, to construct an exact $\mathcal{PT}$ symmetric elastic wave system, one needs both loss and gain. Materials that induce loss are ubiquitous in nature, however, materials that introduce gain are not. Thus, an equivalent gain medium needs to be constructed artificially. There are several methods used to do this in solids that include using piezoelectric materials shunted by negative-resistance circuits [30], electrically biased piezoelectric semiconductors [33], and optomechanical systems derived by optical excitation [42]. Among these methods, due to ease of realization and convenience in tunability, shunted piezoelectric materials are commonly used to get gain in a $\mathcal{PT}$ symmetric elastic wave system [20,21,34]. Using piezoelectric materials with shunted circuits, we design a $\mathcal{PT}$ symmetric metamaterial beam for achieving elastic flexural wave CPAL, and show that the frequency and the periodicity of the CPAL are also linked to the band structure, even in complex multifield coupling elastic systems. Thanks to the tunability of circuits, we demonstrate a unique CPAL that can be induced in the Bragg's bandgap. The design and analysis is based on using Timoshenko beam theory, which provides a means of accurately describing the response at high frequencies. We also develop a semi-analytical reverberation-ray matrix method (RRM) to analyze the scattering properties of the $\mathcal{PT}$ symmetric metamaterial beam, which shows the same fidelity but overcomes numerical instability and poor efficiency of traditional numerical methods, such as the transfer matrix method (TMM) and the finite element method (FEM). The flexural wave propagation is governed by a fourth-order partial differential equation that predicts the existence of intrinsic evanescent waves. The effect of evanescent waves on the CPAL are also investigated.

This paper is arranged as follow: Section II demonstrates the unique transmission and reflection properties of a periodic $\mathcal{PT}$ symmetric metamaterial rod, and explains the relation between the band structure and the periodic-like CPAL observed when changing the cell number. Section III uses Timoshenko beam theory to derives the conditions for observing a $\mathcal{PT}$ symmetric beam, and constructs a $\mathcal{PT}$ symmetric metamaterial beam using unit cells with shunted piezoelectric materials. The section uses the more efficient RRM described in the Appendix to demonstrate how flexural wave CPALs can be predicted from band structure. In addition, the effect of evanescent waves on flexural wave CPALs is discussed. Section IV demonstrates the tunability of the flexural wave CPAL, which can be induced in the Bragg's bandgap. Section V provides the conclusion.

II. THE PERIODIC $\mathcal{PT}$ SYMMETRIC METAMATERIAL ROD

A. Scattering properties

To reveal the link between CPALs and band structure, we first analyze longitudinal wave propagation in a simple periodic $\mathcal{PT}$ symmetric thin rod. The response of the rod in the frequency domain is governed by

$$\omega^2\rho(x)\bar{u}(x,\omega)+\frac{\partial}{\partial x}\left[E(x)\frac{\partial\bar{u}(x,\omega)}{\partial x}\right]=0 \tag{1}$$

for the longitudinal displacement $u(x,t)=\bar{u}(x,\omega)\mathrm{e}^{-\mathrm{i}\omega t}$, where t and ω are, respectively, time and angular frequency, x is the spatial coordinate, $\mathrm{i}^2=-1$, ρ denotes density, and E denotes Young's modulus. Applying the parity operator $\mathcal{P}$ [*i.e.*, $\mathcal{P}\bar{u}(x,\omega)=\bar{u}(-x,\omega)$] and the time reversal operator $\mathcal{T}$ [i.e., $\mathcal{T}\bar{u}(x,\omega)=\bar{u}^*(x,\omega)$ in which "$*$" represents complex conjugate] to Eq. (1) leads to the $\mathcal{PT}$ symmetric conditions for the rod [13,43]. These conditions are given as $\rho(x)=\rho^*(-x)$ and $E(x)=E^*(-x)$. When satisfied, the function $\mathcal{PT}u(x,t)$ is also a solution of Eq. (1). A possible configuration of the N-cell $\mathcal{PT}$ symmetric rod is shown in Fig. 1. Here, $\rho(x)=\rho_0$, and $E(x)=E^*(-x)$ is taken as complex to introduce loss (i.e., $E_l=E_0\mathrm{e}^{-\mathrm{i}\alpha}$) and gain (i.e., $E_g=E_0\mathrm{e}^{\mathrm{i}\alpha}$), with $0<\alpha<\pi/2$. The positive real ρ_0 and E_0 used in constructing the metamaterial are also used as the density and Young's modulus, respectively, of background material outside the N-cell metamaterial rod. The unit cell of the metamaterial rod has a length L and consists of half loss and half gain.

In this case, the displacement amplitude $\bar{u}(x,\omega)$ can be expressed as

$$\bar{u}(x,\omega)=\begin{cases}A_1^-\mathrm{e}^{\mathrm{i}k_0(x+\frac{NL}{2})}+D_1^-\mathrm{e}^{-\mathrm{i}k_0(x+\frac{NL}{2})}, & x\leqslant-\frac{NL}{2},\\ \varphi(x,\omega), & -\frac{NL}{2}\leqslant x\leqslant\frac{NL}{2},\\ D_1^+\mathrm{e}^{\mathrm{i}k_0(x-\frac{NL}{2})}+A_1^+\mathrm{e}^{-\mathrm{i}k_0(x-\frac{NL}{2})}, & x\geqslant\frac{NL}{2},\end{cases} \tag{2}$$

in which $k_0=\omega\sqrt{\rho_0/E_0}$. The transfer matrix $\mathbf{T}$ of one cell of the metamaterial bar is written as $\mathbf{T}=\mathbf{M}_g\mathbf{N}_g\mathbf{M}_g^{-1}\mathbf{M}_l\mathbf{N}_l\mathbf{M}_l^{-1}$

for the state of displacement and stress, in which

$$\mathbf{M}_{l(g)} = \begin{bmatrix} 1 & 1 \\ \mathrm{i}k_{l(g)}E_{l(g)} & -\mathrm{i}k_{l(g)}E_{l(g)} \end{bmatrix},$$
$$\mathbf{N}_{l(g)} = \begin{bmatrix} \mathrm{e}^{\mathrm{i}k_{l(g)}L} & 0 \\ 0 & \mathrm{e}^{-\mathrm{i}k_{l(g)}L} \end{bmatrix},$$

and $k_{l(g)} = \omega\sqrt{\rho_0/E_{l(g)}}$. As a result, the N-cell transfer matrix is $\mathbf{T}^N$. The amplitudes in the background response, as given in Eq. (2), are expressed by the relation $[D_1^+, A_1^+]^T = \mathbf{M}_0^{-1}\mathbf{T}^N\mathbf{M}_0[A_1^-, D_1^-]^T$, in which "$T$" denotes transposition and $\mathbf{M}_0 = [1, 1; \mathrm{i}k_0E_0, -\mathrm{i}k_0E_0]$. This can also be written as

$$[D_1^+, A_1^+]^T = \mathbf{M}^N[A_1^-, D_1^-]^T, \tag{3}$$

in which $\mathbf{M} = \mathbf{M}_0^{-1}\mathbf{T}\mathbf{M}_0$. Applying the $\mathcal{PT}$ operator to the solution given in Eq. (2) yields

$$\mathcal{PT}\bar{u}(x,\omega) = \begin{cases} (D_1^+)^*\mathrm{e}^{\mathrm{i}k_0(x+\frac{NL}{2})} + (A_1^+)^*\mathrm{e}^{-\mathrm{i}k_0(x+\frac{NL}{2})}, & x \leqslant -\frac{NL}{2}, \\ \mathcal{PT}\varphi(x,\omega), & -\frac{NL}{2} \leqslant x \leqslant \frac{NL}{2}, \\ (A_1^-)^*\mathrm{e}^{\mathrm{i}k_0(x-\frac{NL}{2})} + (D_1^-)^*\mathrm{e}^{-\mathrm{i}k_0(x-\frac{NL}{2})}, & x \geqslant \frac{NL}{2}. \end{cases} \tag{4}$$

Thus, one also has $([A_1^-, D_1^-]^T)^* = \mathbf{M}^N([D_1^+, A_1^+]^T)^*$. Taking the complex conjugate and comparing with Eq. (3) shows that a $\mathcal{PT}$-symmetric system satisfies the relation

$$(\mathbf{M}^N)^* = (\mathbf{M}^N)^{-1}. \tag{5}$$

This condition indicates that $\det(\mathbf{M}^N) = \det(\mathbf{T}^N) = 1$, in which $\det(\cdot)$ denotes the determinant.

The scattering matrix of the N-cell metamaterial rod is denoted by $\mathbf{S} = [t_l, r_r; r_l, t_r]$ and defined in this problem as $[D_1^+, D_1^-]^T = \mathbf{S}[A_1^-, A_1^+]^T$, in which t_l and r_l represent, respectively, the transmission and reflection coefficients for waves coming from the left and t_r and r_r represent, respectively, these coming from the right. Therefore, $\mathbf{M}^N$ can be expressed in terms of the transmission and reflection coefficients as $\mathbf{M}^N = [\bar{t} - r_l r_r/\bar{t}, r_r/\bar{t}; -r_l/\bar{t}, 1/\bar{t}]$, in which $\bar{t} = t_l = t_r$ results from $\det(\mathbf{M}^N) = 1$. Following [40,41], using Eq. (5), this leads to

$$\mathbf{M}^N = \begin{bmatrix} 1/\bar{t}^* & r_r/\bar{t} \\ -r_l/\bar{t} & 1/\bar{t} \end{bmatrix},$$

and the scattering relations [40]

$$\bar{t}^*\bar{t} + r_l r_r^* = 1, \tag{6a}$$
$$r_r^*\bar{t} + r_r\bar{t}^* = 0, \tag{6b}$$
$$r_l^*\bar{t} + r_l\bar{t}^* = 0. \tag{6c}$$

Eq. (6) and the fact that $\det(\mathbf{M}^N) = 1$ result in the generalized unitarity relation [39]

$$r_l r_r = \bar{t}^2(1 - 1/|\bar{t}|^2),$$

and unimodularity of the scattering matrix $\det(\mathbf{S}) = 1$ [39].

For the infinite periodic metamaterial rod, using Bloch's theory results in the dispersion equation

$$\det(\mathbf{T} - \mathbf{I}\mathrm{e}^{\mathrm{i}qL}) = 0, \tag{7}$$

in which q is the Bloch wavenumber, and $\mathbf{I}$ is the identity matrix. The matrix $\mathbf{M}$ and the transfer matrix $\mathbf{T}$ have the same eigenvalues, which are denoted by $\eta_{1,2}$, and follow the relation $\eta_1 = 1/\eta_2 = \mathrm{e}^{\mathrm{i}qL}$. Thus, $\eta_1 + \eta_2 = 2\cos(qL)$. Based on Cayley-Hamilton theorem [44,45], the Nth power of the two-by-two unimodular matrix $\mathbf{M}$ can be expressed as [41]

$$\mathbf{M}^N = \frac{1}{\sin(qL)}[\mathbf{M}\sin(NqL) - \mathbf{I}\sin((N-1)qL)] = \begin{bmatrix} \frac{1}{\bar{t}_{N=1}^*}\frac{\sin(NqL)}{\sin(qL)} - \frac{\sin((N-1)qL)}{\sin(qL)} & \frac{r_r^{N=1}}{\bar{t}_{N=1}}\frac{\sin(NqL)}{\sin(qL)} \\ -\frac{r_l^{N=1}}{\bar{t}_{N=1}}\frac{\sin(NqL)}{\sin(qL)} & \frac{1}{\bar{t}_{N=1}}\frac{\sin(NqL)}{\sin(qL)} - \frac{\sin((N-1)qL)}{\sin(qL)} \end{bmatrix},$$

which results in

$$1/|\bar{t}|^2 = (1/|\bar{t}_{N=1}|^2 - 1)\sin^2(NqL)/\sin^2(qL) + 1. \tag{8}$$

This equation relates the Bloch wavenumber to the transmission properties, and also indicates the periodic effect.

The eigenvalues and eigenvectors of the scattering matrix $\mathbf{S}$ are, respectively, $s_{1,2} = \bar{t} \pm \sqrt{r_l r_r}$ and $\mathbf{v}_{1,2} = [\pm\sqrt{r_r}, \sqrt{r_l}]^T$. The exceptional point (EP), at which eigenvalues and eigenvectors degenerate simultaneously, indicates the transition from the $\mathcal{PT}$ symmetric phase ($|\bar{t}| < 1$) to the $\mathcal{PT}$ symmetric broken phase ($|\bar{t}| > 1$), and corresponds to perfect transmission ($|\bar{t}| = 1$) and unidirectional zero reflection ($r_l = 0$ or $r_r = 0$) [18]. According to Eq. (8), $|\bar{t}| < 1$ for $|\bar{t}_{N=1}| < 1$, and $|\bar{t}| > 1$ for $|\bar{t}_{N=1}| > 1$. Thus, the EPs with $|\bar{t}| = 1$ and $|\bar{t}_{N=1}| = 1$ are cell number independent.

B. The relation between Bloch band and periodic-like CPAL

For aluminum ($\rho_0 = 2700$ [kg/m^3] and $E_0 = 70$ [GPa]) and for $L = 0.05$ [m], Figs. 2(a) and 2(b) provide the band structure for different α obtained by selecting frequency and solving the dispersion Eq. (7). When α is a positive real number, the $\mathcal{PT}$ symmetric conditions are satisfied, as shown for $\alpha = 0.1$ or $\alpha = 0.2$, and the Bloch wavenumber is real in the Bloch bands. Interestingly, for the $\mathcal{PT}$ symmetric cases, the Bloch wavenumber cannot reach the Brillouin boundary, as is shown in the inset of Fig. 2(b). If α is a pure imaginary number, the metamaterial rod becomes a common sonic crystal with a Bragg's bandgap marked by the gray area in Figs. 2(a) and 2(b). Calculating the transmittance $|\bar{t}|$ with changing cell number N for the $\mathcal{PT}$ symmetric cases is shown in Figs. 2(c) and 2(d). Remarkably, periodic-like extremely high transmittance appears that relates to cell number N (see red rectangle), and with frequency corresponding to the point of maximum Bloch wavenumber [i.e, the ω of maximum $q(\omega)$] in the Bloch band.

This interesting phenomenon can be understood in terms of Eq. (8). The condition for $|\bar{t}|$ to go to infinity is satisfied when $\sin^2(NqL)/\sin^2(qL)$ tends to $|\bar{t}_{N=1}|^2/(|\bar{t}_{N=1}|^2 - 1)$ in the broken phase. When N changes, $1/\sin^2(qL)$ is the envelope of $\sin^2(NqL)/\sin^2(qL)$, so that the maximum of $\sin^2(NqL)/\sin^2(qL)$ occurs at the maximum $q(\omega)$, as shown in Fig. 2(e). On the other hand, $|\bar{t}_{N=1}|$ has a maximum in the broken phase, as shown in Fig. 2(g), and the value of

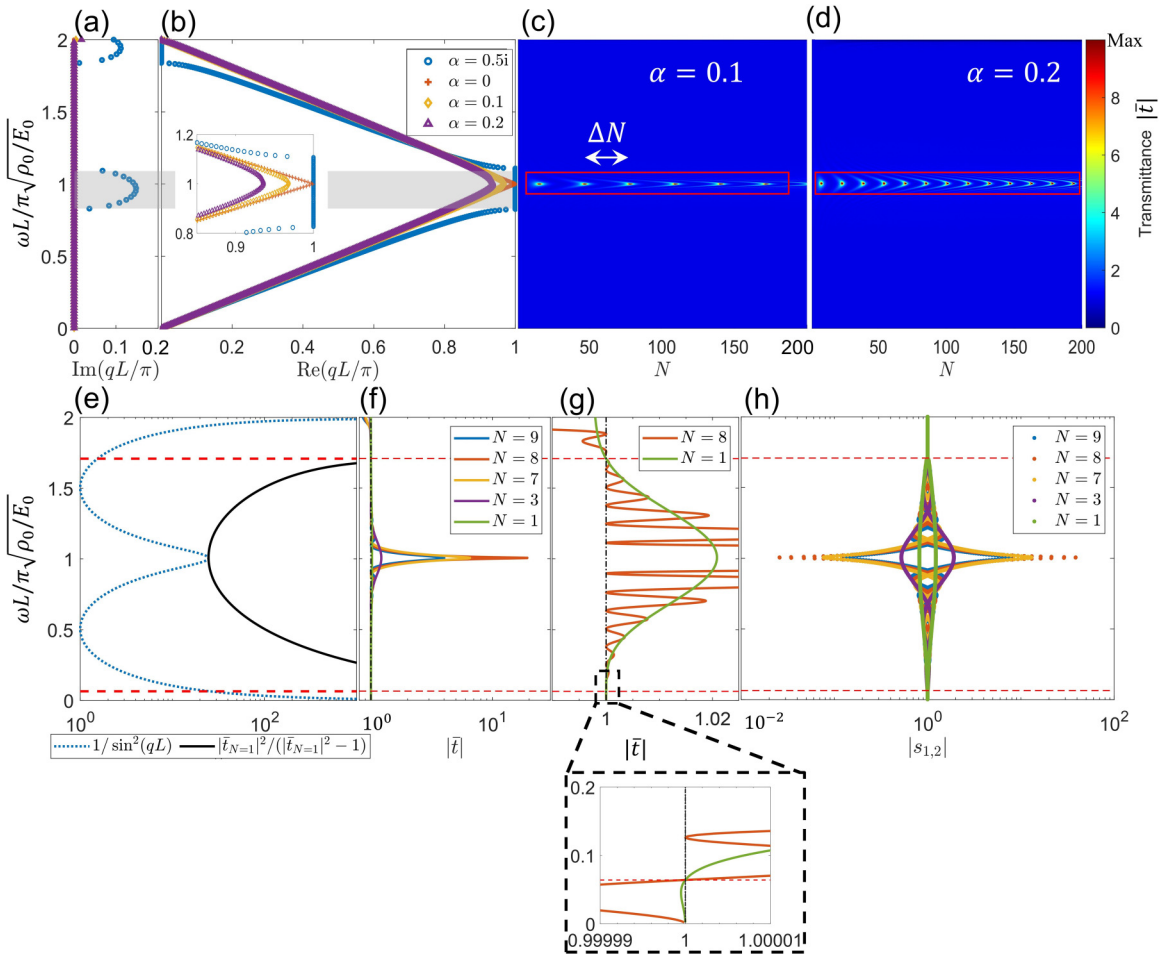

FIG. 2. [(a), (b)] The band structure of metamaterial rods. [(c), (d)] The periodic-like CPAL of the finite periodic metamaterial rod with respect to cell number N relates to the point of maximum real Bloch wavenumber shown in (b). ΔN indicates the interval between two occurrences of CPAL with respect to cell number N. (e) $1/\sin^2(qL)$ and $|\bar{t}_{N=1}|^2/(|\bar{t}_{N=1}|^2 - 1)$ resulting from Eq. (8) with a normalized gain(loss) ratio $\alpha = 0.2$. [(f), (g)] The transmittance of the finite periodic metamaterial rod for given N and $\alpha = 0.2$. (h) The absolute values of the eigenvalues of the scattering matrix for given N and $\alpha = 0.2$. The frequency range between the red-dashed lines represents the $\mathcal{PT}$ symmetric broken phase for $N = 1$.

$|\bar{t}_{N=1}|$ at the frequency of the maximum $q(\omega)$ almost equals the maximum of $|\bar{t}_{N=1}|$, corresponding to the minimum of $|\bar{t}_{N=1}|^2/(|\bar{t}_{N=1}|^2 - 1)$ in the broken phase. These two facts indicate that the CPAL (or quasi-CPAL) occurs at the frequency associated with the maximum Bloch wavenumber. At this frequency, one eigenvalue of the scattering matrix tending to infinite and another tending to zero at the extremely high transmittance, which is the feature of CPAL, such as is shown in Figs. 2(f) and 2(h) for $N = 8$ and $\alpha = 0.2$. The exact CPAL is a singularity of the system, at which the eigenvalues of the scattering matrix are exactly infinite and zero. Changing the cell number can only approach the singularity, achieving quasi-CPAL. This CPAL has no threshold, since, according to our additional numerical study, there exists amplifying effect as long as $\alpha > 0$.

The periodicity of the CPAL with respect to cell number can be estimated as

$$\Delta N = \lfloor \pi/(\pi - \max\{qL\}) \rfloor, \tag{9a}$$

$$\text{or} \quad \Delta N = \lfloor \pi/(\pi - \max\{qL\}) \rfloor + 1, \tag{9b}$$

in terms of $\sin^2(NqL) = 1$ at the maximum Bloch wavenumber, in which $\lfloor \cdot \rfloor$ denotes rounding towards negative infinity, and the minimum cell number for the CPAL is

$$N_{\min} = \lfloor 0.5\pi/(\pi - \max\{qL\}) \rceil, \tag{10}$$

in which $\lfloor \cdot \rceil$ represents the nearest integer function. In this case, the N corresponding to the CPALs are $\{16, 47, 78, 110, 141, 172\}$ for $\alpha = 0.1$ in Fig. 2(c), and $\{8, 23, 39, 54, 70, 85, 101, 116, 132, 147, 163, 178, 194\}$ for $\alpha = 0.2$ in Fig. 2(d). These results agree with those estimated by the Bloch wavenumber given according to Eq. (9) and Eq. (10). They are, with $\Delta N = \lfloor \pi/(\pi - 0.9680\pi) \rfloor = 31$ or $\Delta N = \lfloor \pi/(\pi - 0.9680\pi) \rfloor + 1 = 32$, given by $N_{\min} = \lfloor 0.5\pi/(\pi - 0.9680\pi) \rceil = 16$, for $\alpha = 0.1$, and $\Delta N = \lfloor \pi/(\pi - 0.9355\pi) \rfloor = 15$ or $\Delta N = \lfloor \pi/(\pi - 0.9355\pi) \rfloor + 1 = 16$, by $N_{\min} = \lfloor 0.5\pi/(\pi - 0.9355\pi) \rceil = 8$, for $\alpha = 0.2$. These indicate that the periodicity effect of the CPAL with respect to cell number is similar to a Bragg effect and applicable in more complicated systems, such as considered below in

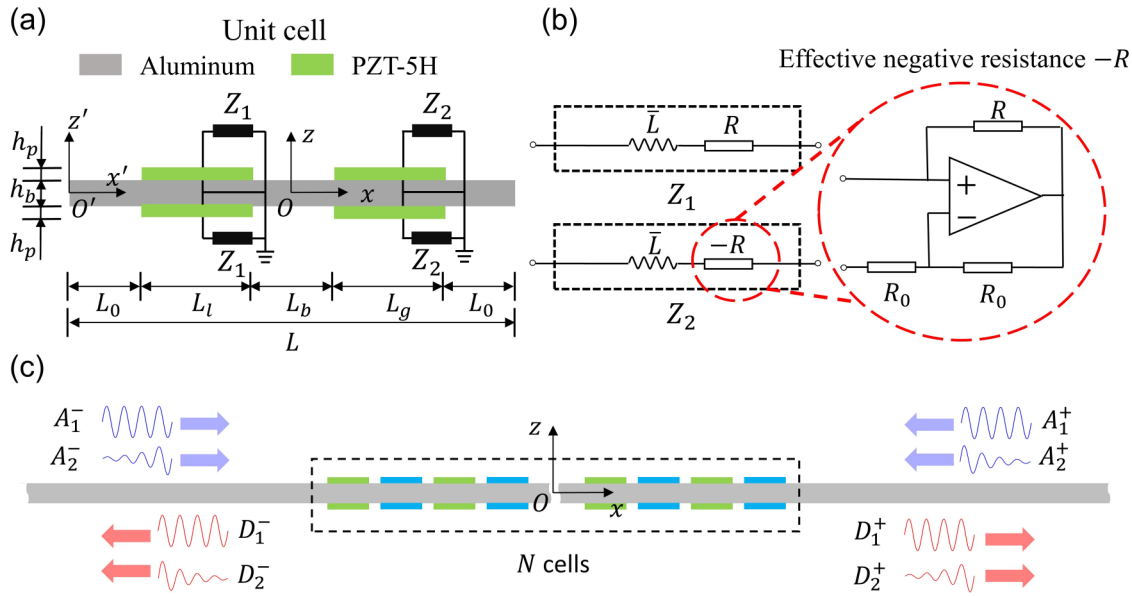

FIG. 3. The $\mathcal{PT}$ symmetric beam. (a) The unit cell of $\mathcal{PT}$ symmetric metamaterial beam with marked geometrical parameters. (b) The electronic circuits with effective impedance Z_1 (an inductor in series with a positive resistor) and Z_2 (an inductor in series with an equivalent negative resistor). (c) The configuration of periodic N-cell $\mathcal{PT}$ symmetric metamaterial beam.

the case of flexural waves in piezoelectric metamaterial beams.

III. THE PERIODIC $\mathcal{PT}$ SYMMETRIC METAMATERIAL BEAM

This section proposes a design methodology for constructing a periodic $\mathcal{PT}$ symmetric metamaterial beam, which uses parameters that can be used in real experiments, and then investigates the scattering properties of flexural waves to reveal the link between the band structure and the periodic flexural wave CPAL effect in fourth-order systems. In the process, the influence of evanescent waves, present in beams, is evaluated.

A. Configuration and $\mathcal{PT}$ symmetric conditions

The unit cell of the metamaterial beam considered here is shown in Fig. 3(a) and constructed by sandwiching an aluminum beam by gluing two pairs of shunted piezoelectric patches that are made of lead zirconate titanate (PZT-5H). The coordinate system Oxz on the figure indicates the sagittal plane of the unit cell. The piezoelectric polarization is assumed to be along z, and wave propagation is to be along x. The aluminum beam has width b and thickness h_b, the left and right pair of piezoelectric patches have lengths L_l and L_g, respectively, width of b, thickness of h_p, and are shunted, respectively, by electronic circuits with effective impedance Z_1 and Z_2. The distance between the patches is L_b, and each patch has a distance of L_0 from the end of the cell.

Considering shear deformation, but neglecting the insignificant piezoelectric effect in shear, the constitutive response of the piezoelectric can be written as

$$\begin{bmatrix} \varepsilon_{xx} \\ \gamma_{xz} \\ D_z \end{bmatrix} = \begin{bmatrix} s_{11}^E & 0 & d_{31} \\ 0 & s_{55}^E & 0 \\ d_{31} & 0 & \epsilon_{33}^\sigma \end{bmatrix} \begin{bmatrix} \sigma_{xx} \\ \tau_{xz} \\ E_z \end{bmatrix},$$

where ε_{xx} and σ_{xx} are, respectively, the axial (normal) strain and stress, γ_{xz} and τ_{xz} are, respectively, the shear strain and stress, D_z and E_z are, respectively, the electric displacement and field intensity along z, and where the material parameters are s_{11}^E, s_{55}^E, d_{31} and ϵ_{33}^σ, which are given for PZT-5H in Table I. The normal compliance of the piezoelectric shunted patch circuit with electrical impedance Z, using the excitation time component $e^{-i\omega t}$, can be written as

$$\bar{s}_{11}^E = s_{11}^E + \frac{i\omega Z d_{31}^2 b_p L_p h_p}{1 - i\omega Z C_p^\sigma}, \tag{11}$$

in which $C_p^\sigma = \epsilon_{33}^\sigma b_p L_p / h_p$ is the capacitance of the piezoelectric at constant stress [47]. This allows the constitutive relation for the shunted piezoelectric patch under dynamic harmonic loading with frequency ω to be rewritten in the form used for linear elastic response (i.e., in a form similar to that of aluminum) [48]. This form is written as

$$\begin{bmatrix} \sigma_{xx} \\ \tau_{xz} \end{bmatrix} = \begin{bmatrix} E_p & 0 \\ 0 & G_p \end{bmatrix} \begin{bmatrix} \varepsilon_{xx} \\ \gamma_{xz} \end{bmatrix} = \begin{bmatrix} 1/\bar{s}_{11}^E & 0 \\ 0 & 1/s_{55}^E \end{bmatrix} \begin{bmatrix} \varepsilon_{xx} \\ \gamma_{xz} \end{bmatrix}, \tag{12}$$

where $E_p(\omega)$ and G_p are effective moduli.

Using Timoshenko beam theory [49,50], the displacements $u(x,z,t)$ along the x direction and $w(x,z,t)$ along the z direction are assumed to be expressed as $u(x,z,t) = -z\theta(x,t)$ and $w(x,z,t) = w(x,t)$, in which $\theta(x,t)$ is the rotation angle resulting from bending of the beam. This induces both axial and shear strains that are given, respectively, by

TABLE I. Material constants for aluminum [5] and lead zirconate titanate (PZT-5H) [46].

Name	Symbol	Value	Unit
Aluminum			
Young's modulus	E_0	70	GPa
Shear modulus	G_0	26.3	GPa
Density	ρ_0	2700	kg/m^3
Lead zirconate titanate (PZT-5H)			
Compliance at constant electric field			
normal	s_{11}^E	1.65×10^{-11}	Pa^{-1}
shear	s_{55}^E	4.35×10^{-11}	Pa^{-1}
Piezoelectric coefficient	d_{31}	-2.74×10^{-10}	C/N
Dielectric constant under zero stress	ε_{33}^σ	3.01×10^{-8}	F/m
Density	ρ_p	7500	kg/m^3

$\varepsilon_{xx}(x,t) = -z\theta'(x,t)$ and $\gamma_{xz}(x,t) = w'(x,t) - \theta(x,t)$, where "$'$" indicates a derivative with respect to x. The resulting dynamical response written in the frequency domain, with $w(x,t) = W(x,\omega)e^{-i\omega t}$, then becomes

$$GA\kappa EIW'''' + (GA\kappa\rho I + mEI)\omega^2 W'' + (\rho I\omega^2 - GA\kappa)m\omega^2 W = 0, \tag{13}$$

in which m denotes mass per unit length, ρI denotes mass moment of inertia per unit length along the bar calculated about the y axis,

$$EI = \begin{cases} E_0 I_0, & \text{Substrate beam,} \\ (EI)_L, \quad (EI)_L = E_0 I_0 + 2E_p^l[I_p + b_p h_p (h_b + h_p)^2/4], & Z_1 \text{ sandwiched beam,} \\ (EI)_G, \quad (EI)_G = E_0 I_0 + 2E_p^g[I_p + b_p h_p (h_b + h_p)^2/4], & Z_2 \text{ sandwiched beam,} \end{cases}$$

$$GA\kappa = \begin{cases} G_0 b h_b \kappa_b, & \text{Substrate beam,} \\ G_0 b h_b \kappa_b + 2G_p b_p h_p \kappa_p, & \text{Sandwiched beam,} \end{cases}$$

$$m = \begin{cases} \rho_0 h_b b, & \text{Substrate beam,} \\ \rho_0 b h_b + 2\rho_p b_p h_p, & \text{Sandwiched beam,} \end{cases}$$

$$\rho I = \begin{cases} \rho_0 I_0, & \text{Substrate beam,} \\ \rho_0 I_0 + 2\rho_p[I_p + b_p h_p (h_b + h_p)^2/4], & \text{Sandwiched beam,} \end{cases}$$

in which E_0, G_0 and ρ_0 are, respectively, Young's modulus, shear modulus, and density of the substrate (aluminum; given in Table I), E_p^l and E_p^g are the effective Young's moduli of, respectively, the left and right piezoelectric patches that are shunted, respectively, by Z_1 and Z_2, $I_0 = \frac{1}{12}h_b^3 b_b$, $I_p = \frac{1}{12}h_p^3 b_p$, κ_b and κ_p are adjustment coefficients associated with the shear stress for, respectively, the substrate and piezoelectric material given by $\kappa_b = 10(1+\upsilon_b)/(12+11\upsilon_b)$, $\kappa_p = 10(1+\upsilon_p)/(12+11\upsilon_p)$, where $\upsilon_b = 1 - \frac{E_0}{2G_0}$ and $\upsilon_p = 1 - \frac{1}{2\tilde{s}_{11}^E G_p}$ [50]. If the rotary inertia effect and shear deformations are neglected, the flexural wave motion in the beam is described by traditional Euler's beam theory, as [50]

$$EIW'''' - \rho A\omega^2 W = 0. \tag{14}$$

Applying the $\mathcal{PT}$ operator to Eq. (13) leads to the $\mathcal{PT}$ symmetric conditions for the beam given as

$$m(x) = [m(-x)]^*, \tag{15a}$$

$$GA\kappa(x) = [GA\kappa(-x)]^*, \tag{15b}$$

$$\rho I(x) = [\rho I(-x)]^*, \tag{15c}$$

$$EI(x) = [EI(-x)]^*. \tag{15d}$$

Since the parameters m, $GA\kappa$, and ρI are real, the first three equations are satisfied when $L_l = L_g$. According to Eqs. (11), (12), and (14), the fourth condition given in Eq. (15) is satisfied when $L_l = L_g$ and $iZ_1 = (iZ_2)^*$. For the following, the material properties are given in Table I and the geometric design parameters considered for the unit cell are given in Table II. For these parameters and properties, if one takes the resistances $Z_1 = -Z_2 = R = 500\ \Omega$, the $\mathcal{PT}$ symmetry conditions are satisfied and result in the effective parameters $(EI)_L$ and $(EI)_G$ plotted in Fig. 4. The real and the imaginary parts of these two effective parameters have the relations $\mathrm{Re}((EI)_L) = \mathrm{Re}((EI)_G)$ and $\mathrm{Im}((EI)_L) = -\mathrm{Im}((EI)_G)$. An

TABLE II. Geometric parameters (unit:mm).

b	h_b	h_p	L_0	L_b	L_l	L_g
40	0.8	0.8	10	20	30	30

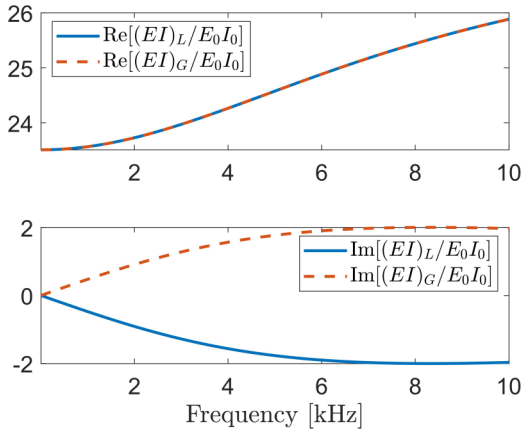

FIG. 4. The effective parameters of the metamaterial beam in the sandwiched part with $R = 500\ \Omega$. Solid lines represent loss, and dashed lines represent gain.

effective impedance Z_2 with negative resistance can be realized using an equivalent negative resistance circuit, as shown in Fig. 3(b), in which an operational amplifier is needed with connection to an external power source.

B. Complex band structure

The harmonic wave solution $W(x, \omega)$ can be rewritten as

$$W(x, \omega) = C_1 e^{\lambda x}, \tag{16}$$

in which C_1 is the wave amplitude. Substituting Eq. (16) into Eq. (13) leads to the characteristic equation

$$GA\kappa EI\lambda^4 + (GA\kappa\rho I + mEI)\omega^2\lambda^2 + (\rho I\omega^2 - GA\kappa)m\omega^2 = 0,$$

that can be solved analytically to get

$$\lambda_1 = -i\sqrt{\frac{m\omega^2 EI + GA\kappa\omega^2\rho I + \sqrt{\Delta}}{2GA\kappa EI}},$$

$$\lambda_2 = -i\sqrt{\frac{m\omega^2 EI + GA\kappa\omega^2\rho I - \sqrt{\Delta}}{2GA\kappa EI}},$$

$$\lambda_3 = -\lambda_1, \quad \lambda_4 = -\lambda_2.$$

in which $\Delta = (mEI - GA\kappa\rho I)^2\omega^4 + 4(GA\kappa)^2 m\omega^2 EI$. Therefore, the solution takes the form

$$W(x, \omega) = a_1 e^{\lambda_1 x} + a_2 e^{\lambda_2 x} + d_1 e^{\lambda_3 x} + d_2 e^{\lambda_4 x}. \tag{17}$$

Using the $O'x'z'$ coordinate system, as shown in Fig. 3(a), the state vector of the beam at x', given as $\mathbf{X}(x') = [\text{deflection, rotating angle, bending moment, shear force}]^T = [W,\ \Theta,\ M,\ Q]^T$, can be expressed in the form

$$\mathbf{X}(x') = \mathbf{A}(x')\mathbf{a} + \mathbf{D}(x')\mathbf{d}, \tag{18}$$

for

$$\mathbf{A}(x') = \begin{bmatrix} e^{\lambda_1 x'} & e^{\lambda_2 x'} \\ c_1 e^{\lambda_1 x'} & c_2 e^{\lambda_2 x'} \\ EIc_1\lambda_1 e^{\lambda_1 x'} & EIc_2\lambda_2 e^{\lambda_2 x'} \\ GA\kappa(\lambda_1 - c_1)e^{\lambda_1 x'} & GA\kappa(\lambda_2 - c_2)e^{\lambda_2 x'} \end{bmatrix},$$

$$\mathbf{D}(x') = \begin{bmatrix} e^{\lambda_3 x'} & e^{\lambda_4 x'} \\ c_3 e^{\lambda_3 x'} & c_4 e^{\lambda_4 x'} \\ EIc_3\lambda_3 e^{\lambda_3 x'} & EIc_4\lambda_4 e^{\lambda_4 x'} \\ GA\kappa(\lambda_3 - c_3)e^{\lambda_3 x'} & GA\kappa(\lambda_4 - c_4)e^{\lambda_4 x'} \end{bmatrix},$$

$$\mathbf{a} = \begin{bmatrix} a_1 \\ a_2 \end{bmatrix}, \quad \mathbf{d} = \begin{bmatrix} d_1 \\ d_2 \end{bmatrix},$$

in which $c_i = \frac{m\omega^2 + GA\kappa\lambda_i^2}{GA\kappa\lambda_i}$ for $i = 1, 2, 3, 4$, and the parameters EI, $GA\kappa$, m, and ρI change along the unit cell. For each length L_i with constant parameters, the transformation matrix takes the form

$$\mathbf{T}_i = [\mathbf{A}_i(L_i)\ \mathbf{D}_i(L_i)][\mathbf{A}_i(0)\ \mathbf{D}_i(0)]^{-1}.$$

The transfer matrix for the entire unit cell, as shown in Fig. 3(a), then becomes

$$\mathbf{T} = \mathbf{T_0}\mathbf{T_p^l}\mathbf{T_b}\mathbf{T_p^g}\mathbf{T_0},$$

where $\mathbf{T_0}$ and $\mathbf{T_b}$ are transformations for, respectively, the substrate-only segments of length L_0 and L_b, and $\mathbf{T_p^l}$ and $\mathbf{T_p^g}$ are transformations for, respectively, the sandwiched segments with lengths L_l and L_g. The periodic Bloch's theorem provides the dispersion equation of the metamaterial beam as

$$|\mathbf{T} - e^{iqL}\mathbf{I}| = 0, \tag{19}$$

in which q denotes the Bloch wave number for flexural wave.

Dispersion equation (19) results in the band structures shown in Fig. 5, as given for the short circuit case [$Z_1 = Z_2 = 0$, Figs. 5(a) and 5(b)] and the $\mathcal{PT}$ symmetric case [$Z_1 = -Z_2 = 1000\ \Omega$, Figs. 5(c) and 5(d)]. The gray areas in the figure represent Bragg's bandgaps where the Bloch wave number is imaginary. For comparison, the results based on Euler beam theory and based on FEM analysis are also shown in the figure. The FEM analysis is conducted by the commercial software Comsol Multiphysics, assuming plane stress and using serendipity quadrilateral elements. Because of the shunted piezo patches in metamaterial model, we use the solid mechanics module, electrostatics module and electrical circuit module in Comsol. The mechanical response and electrical response of piezo patches are unified by the piezoelectric effect interface. The shunted circuits are set in the electrical circuit module, and are connected to electrostatics module through terminal interfaces.

Comparing theories based on the Euler and Timoshenko beam theories to the more accurate FEM results indicates that the Timoshenko beam theory clearly captures the high frequency response much more accurately. In addition, the solution indicates a transition in the third Bloch band (6–9 kHz) from the short circuit case that the Bloch wavenumber q can reach the boundary $q = \pi/L$ to the $\mathcal{PT}$ symmetric case where q cannot reach π/L, as shown by comparing Fig. 5(a) and (c). This is further supported by the FEM solution, that indicates the eigenfrequency becomes a complex number for the $\mathcal{PT}$ symmetric case, and that there exists a band EP indicating the block Bloch bands degenerate, as shown in the insets of Fig. 5(c). In particular, the inset identified by a red dashed outline shows the development of the

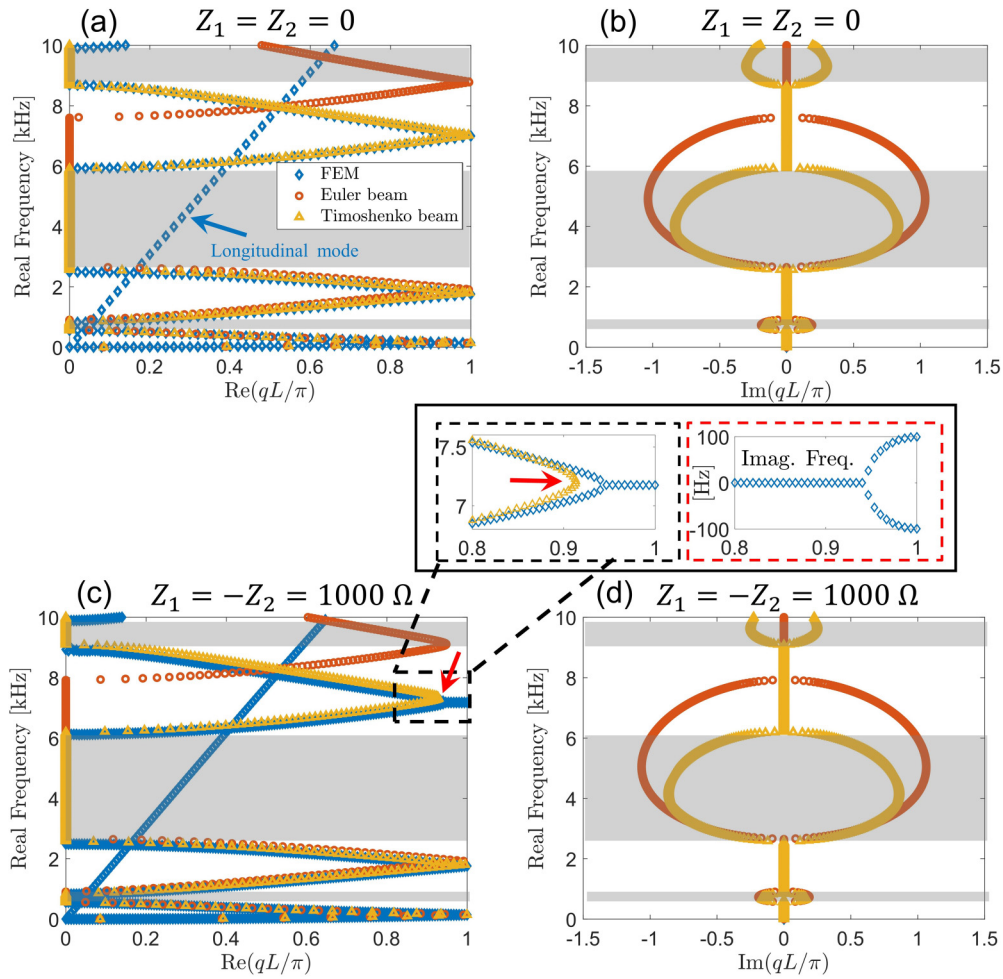

FIG. 5. Band structures of the infinite periodic metamaterial beam. [(a), (b)] Short circuit case ($Z_1 = -Z_2 = R = 0$). [(c), (d)] $\mathcal{PT}$ symmetric case ($Z_1 = -Z_2 = R = 1000\ \Omega$). [(b), (d)] Show only that the imaginary components of the band structure obtained by solving the dispersion equation (19) given frequency. The insets in (c) indicate the real and imaginary components of the eigenfrequency calculated by FEM. FEM calculates eigenfrequency given wavenumber. The analytical results are obtained by solving for the wavenumber given frequency.

imaginary part of eigenfrequency in the FEM analysis. Comparison of the FEM obtained EP and the solution obtained from the dispersion equation (19) indicates that the maximum Bloch wavenumber, identified by red arrows in Fig. 5(c), corresponds to the band EP obtained in FEM by solving for frequency given wavenumber. When the Bloch wavenumber is smaller than band EP, the wavenumber and the frequency of dispersion curves are pure real, and the dispersion curves in the both scenarios, solving for wavenumber and solving for frequency, should agree totally. However, Timoshenko's beam model is also an approximation theory, which gives rise to the small difference between the analytical and the FEM. Following the analysis described for the $\mathcal{PT}$ symmetric metamaterial rod, the flexural wave CPAL gets induced at the frequency associated with the maximum Bloch wavenumber.

C. The periodic flexural wave CPAL

Figure 3(c) shows the finite periodic N-cell $\mathcal{PT}$ symmetric metamaterial beam sandwiched between two semi-infinite aluminum beams, which function as the background medium. The wave field in the background mediums and metamaterial beam can be expressed as

$$W(x,\omega) = \begin{cases} A_1^- e^{\lambda_3(x+\frac{NL}{2})} + A_2^- e^{\lambda_4(x+\frac{NL}{2})} + D_1^- e^{\lambda_1(x+\frac{NL}{2})} + D_2^- e^{\lambda_2(x+\frac{NL}{2})}, & x \leqslant -\frac{NL}{2}, \\ \phi(x,\omega), & -\frac{NL}{2} < x < \frac{NL}{2}, \\ A_1^+ e^{\lambda_1(x-\frac{NL}{2})} + A_2^+ e^{\lambda_2(x-\frac{NL}{2})} + D_1^+ e^{\lambda_3(x-\frac{NL}{2})} + D_2^+ e^{\lambda_4(x-\frac{NL}{2})}, & x \geqslant \frac{NL}{2}, \end{cases}$$

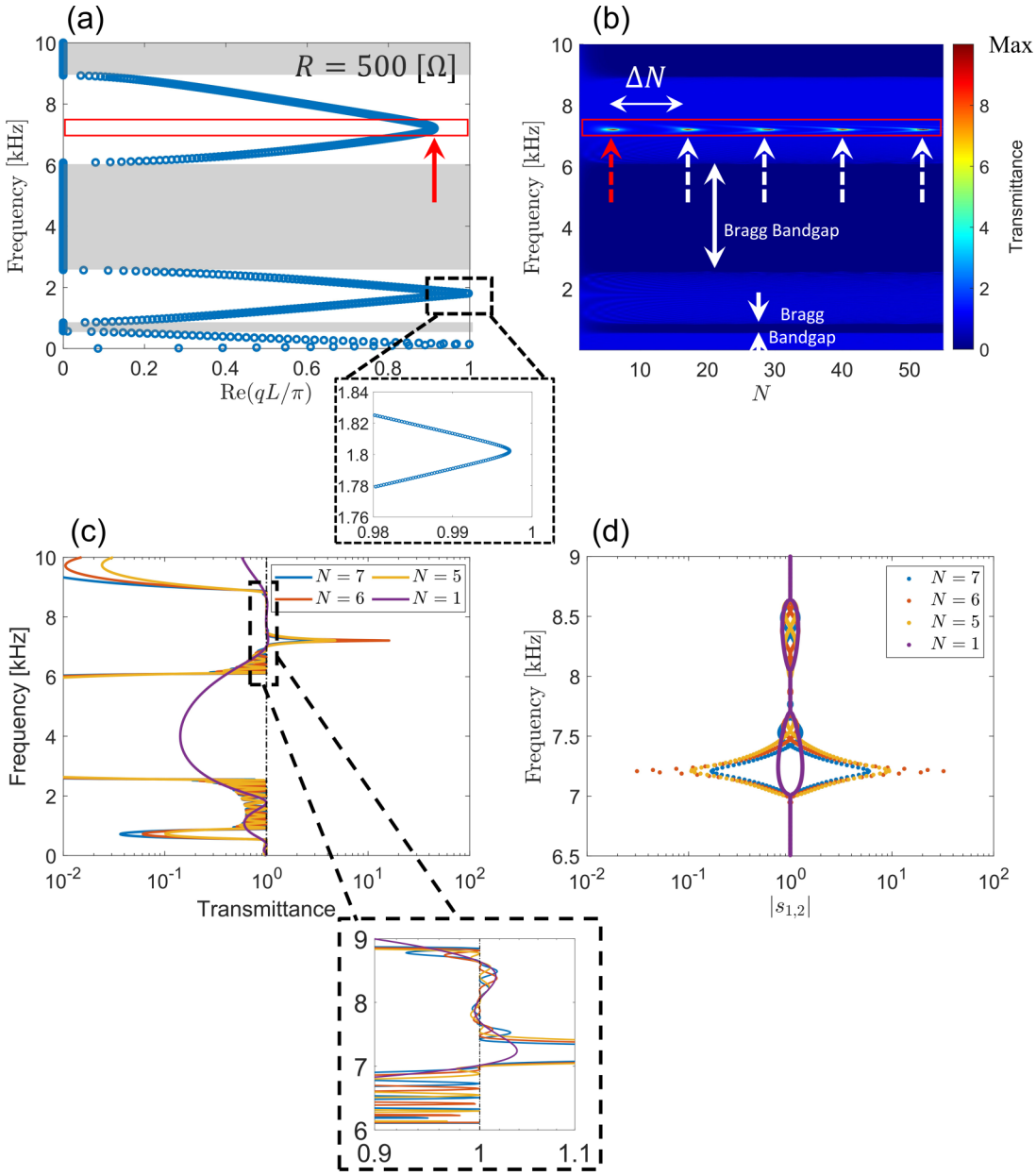

FIG. 6. The band structure and scattering properties of a $\mathcal{PT}$ symmetric metamaterial beam with $Z_1 = -Z_2 = R = 500\ \Omega$. (a) The band structure from Eq. (19), on which the red-solid arrow indicates the maximum wavenumber. (b) The transmittance varying cell number, on which the dashed arrows represent the CPALs, and the red arrow denotes the CPAL with minimum cells. (c) The transmittance and (d) the eigenvalues of scattering matrix **S** with noted cell numbers. The red-solid rectangles indicate the same frequency as in (a) and (b).

in which A_1^-, A_1^+, D_1^-, D_1^+ are the amplitudes of the propagation waves, and A_2^-, A_2^+, D_2^-, D_2^+ are the amplitudes of the evanescent waves. The resulting input amplitude vector $\mathbf{a_s}$ and output amplitude vector $\mathbf{d_s}$ are defined as

$$\mathbf{a_s} = [A_1^-, A_2^-, A_1^+, A_2^+]^T, \quad \mathbf{d_s} = [D_1^-, D_2^-, D_1^+, D_2^+]^T. \tag{20}$$

The existence of evanescent wave in the beam results in a 4×4 scattering matrix $\mathbf{S^r}$ with the elements on the principal diagonal representing reflection coefficients. For an N-cell metamaterial, the fourth-order scattering matrix $\mathbf{S^r}$ can be explicitly and efficiently calculated by RRM. The detailed derivation is provided in Appendix. Only propagating waves in the far field in the background media lead to the scattering matrix of propagating waves, which can be written as

$$\mathbf{S} = \begin{bmatrix} t_l & r_r \\ r_l & t_r \end{bmatrix} = \begin{bmatrix} S_{31}^r & S_{33}^r \\ S_{11}^r & S_{13}^r \end{bmatrix}, \quad \begin{bmatrix} D_1^+ \\ D_1^- \end{bmatrix} = \mathbf{S} \begin{bmatrix} A_1^- \\ A_1^+ \end{bmatrix}. \tag{21}$$

Setting $Z_1 = -Z_2 = R = 500\ \Omega$, Figs. 6(a) and 6(b) shows, respectively, the band structure obtained by solving Eq. (19) and the transmittance resulting from varying the cell number N. Surprisingly, even in the more complicated piezoelectric metamaterial beam, a periodic-like high transmittance flexural wave CPAL appears, and its frequency corresponds to the frequency at the point of maximum Bloch wavenumber in the Bloch band that cannot reach to Brillouin boundary (i.e., $q\pi/L = 1$). This follows since this

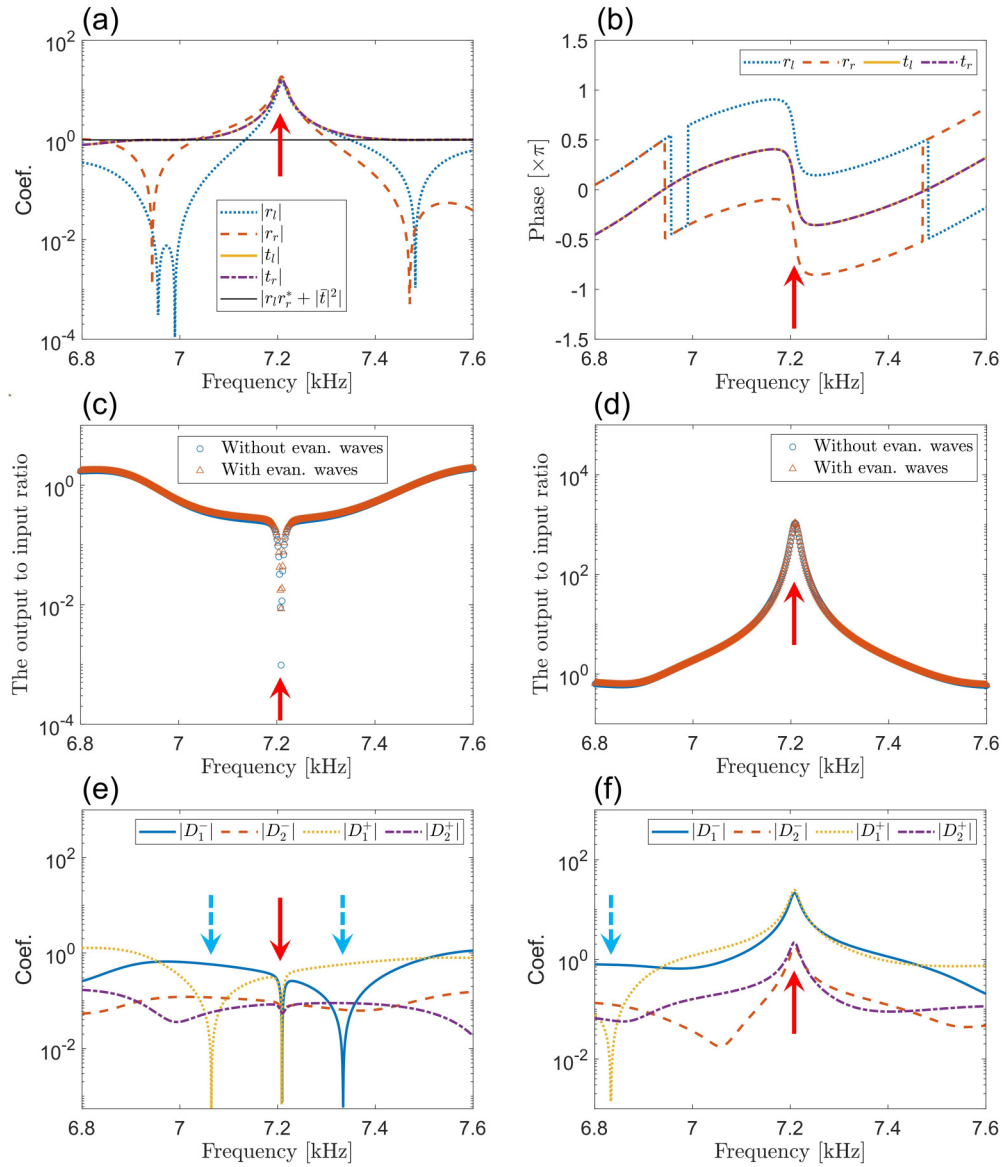

FIG. 7. The scattering properties of the 6-cell $\mathcal{PT}$ symmetric metamaterial beam. (a) The transmittance and reflectance for propagating waves. (b) The phases of transmission and reflection. [(c), (d)] The output to input ratio of energy for absorber and laser, respectively. [(e),(f)] The amplitudes of outgoing waves for absorber and laser, respectively. The red arrows indicate the frequency of the flexural wave CPAL, and the blue-dashed arrows indicate the unidirectional reflectionlessness.

phenomenon is an interference effect. The cell number N of these periodic CPAL are {6, 17, 29, 40, 52}, and the maximum Bloch wavenumber, indicated by a red arrow in Fig. 6(a), is $0.9133\pi/L$ at 7.197 kHz. These are linked by Eq. (9) (i.e., $\triangle N = \lfloor \pi/(\pi - 0.9133\pi) \rfloor = 11$ or $\triangle N = \lfloor \pi/(\pi - 0.9133\pi) \rfloor + 1 = 12$). According to Eq. (10), the minimum cell number to achieve the flexural wave CPAL is $N_{\min} = \lfloor 0.5\pi/(\pi - 0.9133\pi) \rceil = 6$ in agreement with the results in Figs. 6(c) and 6(d). It is worth noting that the low-frequency band still cannot reach the boundary, as shown in the inset of Fig. 6(a), but is close. It takes more cells to achieve the CPAL, as $N_{\min} = \lfloor 0.5\pi/(\pi - 0.9972\pi) \rceil = 179$ at 1.8 kHz. Changing the value R, the minimum N and the interval $\triangle N$ can be made smaller as the CPALs in Figs. 2(b) and 2(c) show. However, in this piezoelectric metamaterial beam, these are not a monotonic function of R since the loss and gain are not monotonic in R. In short, the CPAL is predictable using only the band structure of the infinite periodic beam to identify the frequency of periodicity. It is worth mentioning that, besides the flexural mode in beam, longitudinal and torsional modes also exist. We conducted additional three-dimensional FEM analysis, which shows there are band EPs of longitudinal modes, but no band EP for the torsional modes. This implies that our piezoelectric beam metamaterial cannot achieve torsional wave CPAL.

D. The effect of evanescent wave

The CPAL can act as a multifunctional device, amplifier, absorber and laser, depending on the nature of the incident waves. At the CPAL, when the incident wave comes from only one side, either the left or the right, the transmittance

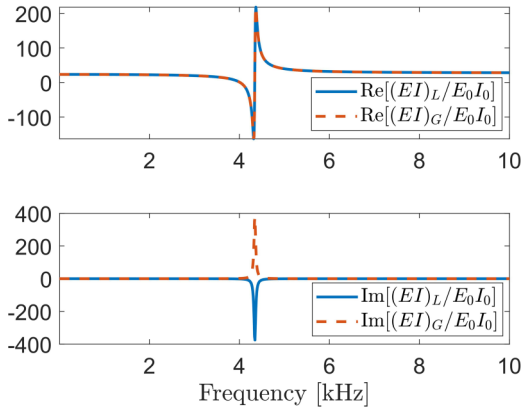

FIG. 8. The effective parameters of the metamaterial beam in the sandwiched part with $R = 10\ \Omega$ and $f_{LC} = 4$ kHz. Solid lines represent loss, and dashed lines represent gain.

and reflectance simultaneously become extremely high, as shown in Fig. 7(a). The phases of the transmission and the reflection change by π in the frequency domain near this point, as shown in Fig. 7(b). If the input signals are simultaneously excited at both sides of the $\mathcal{PT}$ symmetric metamaterial beam, there is an additional degree of freedom that can be used to manipulate the system. The two-by-two scattering matrix $\mathbf{S}$ of the propagating waves has normalized eigenvectors $\mathbf{v}_{1,2} = [1,\ \pm\sqrt{r_l/r_r}]^T/\sqrt{1+|r_l|/|r_r|}$ corresponding to eigenvalues $s_{1,2}$. At the CPAL, for $N = 6$, there is a minimum eigenvalue $|s_1| \ll 1$ and a maximum eigenvalue $|s_2| \gg 1$, as shown in Fig. 6(d). Therefore, when the input amplitude vector $\mathbf{a_s} = [A_1^-, A_2^-, A_1^+, A_2^+]^T$ is given by $\mathbf{a_s} = [1,\ 0,\ \sqrt{r_l/r_r}, 0]^T/\sqrt{1+|r_l|/|r_r|}$, based on Eq. (21), the elements corresponding to propagating waves in the output amplitude vector are $D_1^+ = s_1/\sqrt{1+|r_l/r_r|}$ and $D_1^- = s_1\sqrt{r_l/r_r}/\sqrt{1+|r_l/r_r|}$, and the output to input ratio of energy of the propagating waves is $|s_1|^2$. The eigenvalue $|s_1| \ll 1$ leads to an absorber at the frequency of 7.207 kHz, indicated by a red arrow in Fig. 7(c). On the contrary, when the input amplitude vector $\mathbf{a_s} = [1,\ 0, -\sqrt{r_l/r_r}, 0]^T/\sqrt{1+|r_l/r_r|}$, the elements of the output amplitude vector become $D_1^+ = s_2/\sqrt{1+|r_l/r_r|}$ and $D_1^- = s_2\sqrt{r_l/r_r}/\sqrt{1+|r_l/r_r|}$. This achieves the laser shown in Fig. 7(d) for $|s_2| \gg 1$. It should be noted that the amplitudes of evanescent waves in the input amplitude vector $\mathbf{a_s}$ are set to zero. This is consistent with the general understanding that the precise control of induced evanescent waves is hard

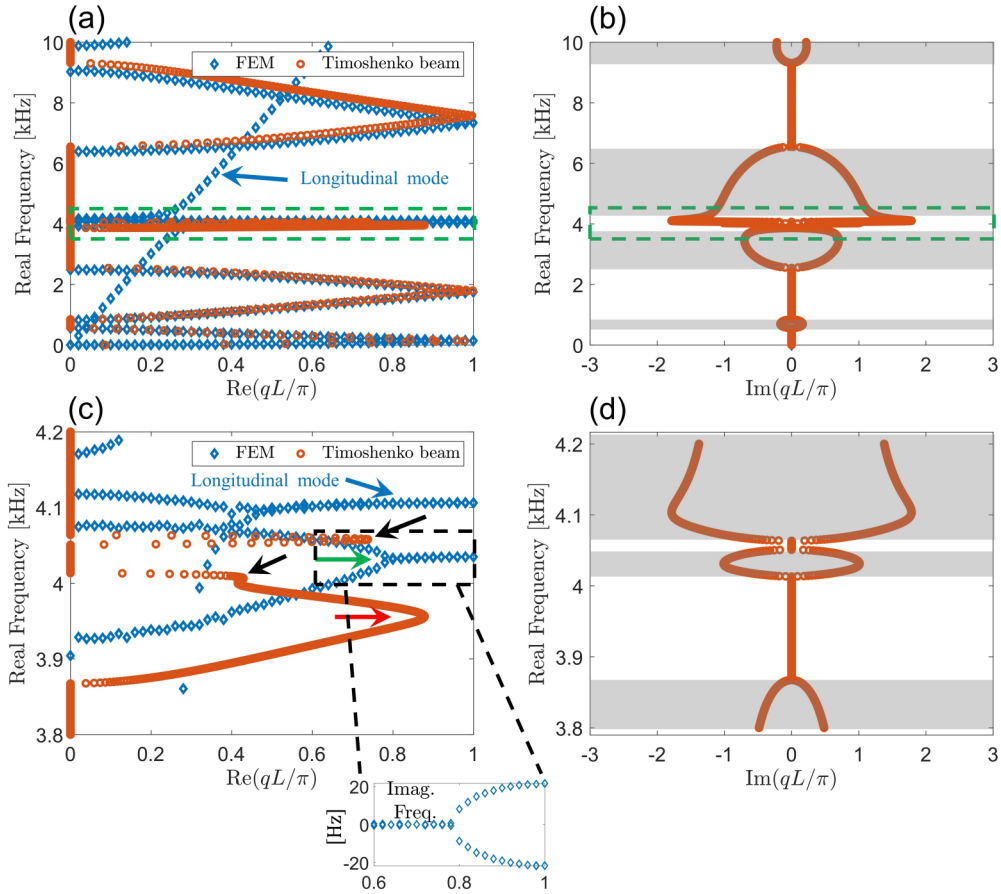

FIG. 9. The band structures of a $\mathcal{PT}$ symmetric metamaterial beam with resistors and inductors (the resistance $R = 10\ \Omega$ and resonant frequency $f_{LC} = 4$ kHz). [(a), (c)] The real parts of band structure given by Eq. (19) and FEM. [(b), (d)] Represent the imaginary parts corresponding to the real band structures in (a) and (c) obtained by solving Eq. (19), respectively. [(c), (d)] Expanded portions indicated by the green dashed squares in (a) and (b). The inset in (c) is the corresponding imaginary parts calculated by FEM. The green arrow indicate the band EP (FEM), and the black and red arrows indicate the maximum wavenumbers (Timoshenko beam theory).

in practice, but the control of propagating waves is easily implemented. The output energy with evanescent waves (D_2^- and D_2^+), based on Eq. (A10), results in an output to input ratio of energy, $||\mathbf{S}^{\mathbf{r}}\mathbf{a}_{\mathbf{s}}||^2/||\mathbf{a}_{\mathbf{s}}||^2$, for the absorber and laser as shown, respectively, in Figs. 7(c) and 7(d). The results indicate that the influence of the evanescent waves is relatively insignificant, even in the near field. In general, the amplitudes of evanescent waves are about one order smaller than that of propagating waves, as shown in Figs. 7(d) and 7(e), except for the points indicated by the blue dash arrows, at which the system interestingly acts as an unidirectional output device.

IV. TUNABLE SCATTERING PROPERTIES: FLEXURAL WAVE CPAL IN THE BRAGG'S BANDGAP

A distinct advantage of piezoelectric metamaterials is that the effective material parameters are highly tunable due to the diverse tunable circuits. When an inductor is introduced in series with either the positive resistor or effective negative resistor in their associated circuits, as shown in Fig. 3(b), the circuit and the piezoelectric patch can form an *RLC* resonance circuit with the resonant frequency $f_{LC} = \frac{1}{2\pi\sqrt{\bar{L}C_p^{\sigma}}}$, in which $\bar{L}$ is inductance, and

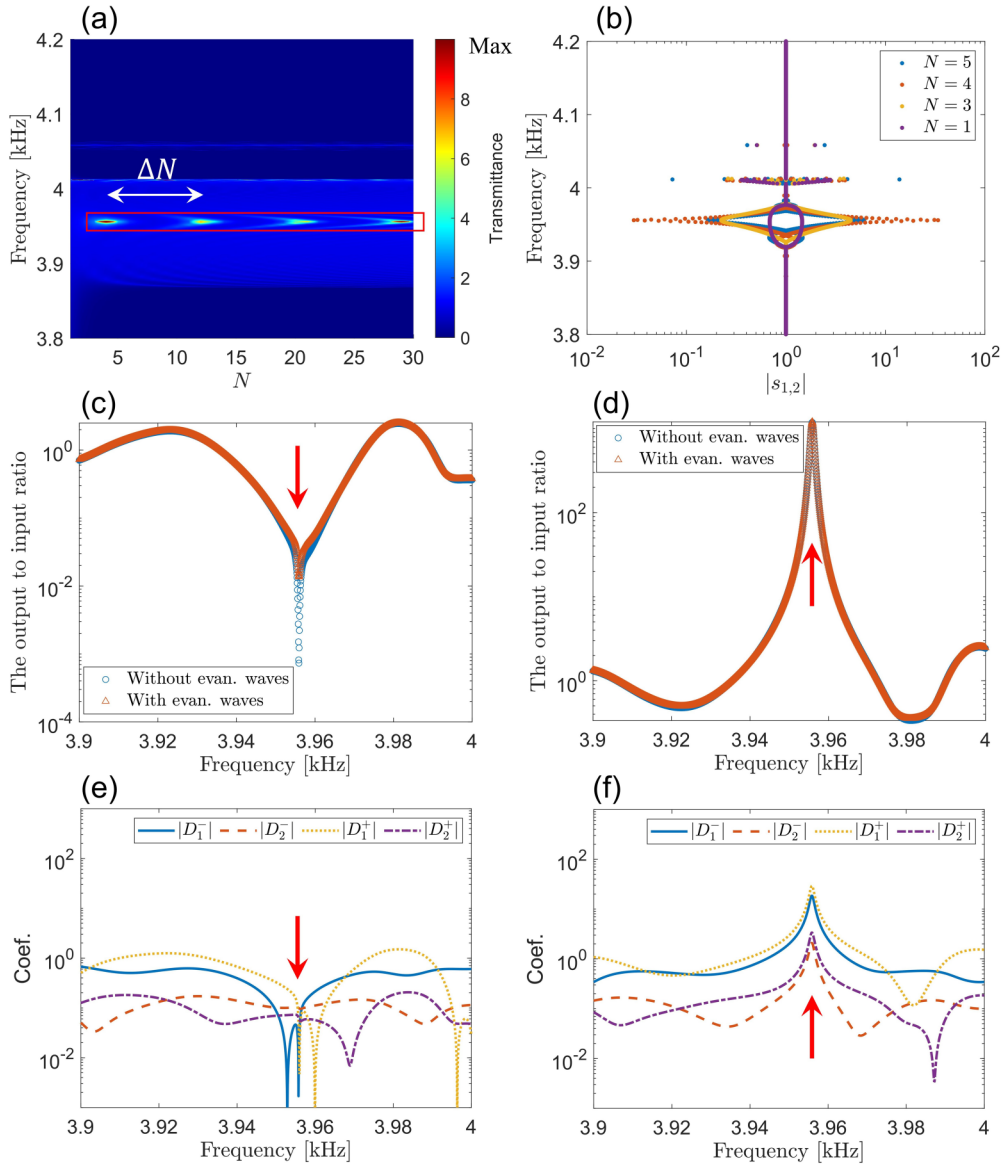

FIG. 10. The scattering properties of $\mathcal{PT}$ symmetric metamaterial beam with resistors and inductors (the resistance $R = 10\ \Omega$ and resonant frequency $f_{LC} = 4$ kHz). (a) The transmittance for varying cell number. ΔN indicates the interval between two CPALs with respect to cell number N. The CPALs are marked by the red box. (b) The eigenvalues of two-by-two scattering matrix $\mathbf{S}$ for different cell number N. [(c), (d)] The output to input ratio of energy for absorber and laser, respectively. [(e), (f)] The amplitudes of outgoing waves for the absorber and laser, respectively. The red arrows indicate the frequency of the flexural wave CPAL.

one gets $Z_1 = R - \mathrm{i}\omega\bar{L}$ and $Z_2 = -R - \mathrm{i}\omega\bar{L}$. With these shunt circuits, the metamaterial beam can also be $\mathcal{PT}$ symmetric for the case $\mathrm{i}Z_1 = (\mathrm{i}Z_2)^*$ and requiring the effective parameters $(EI)_L$ and $(EI)_G$ having the relations $\mathrm{Re}((EI)_L) = \mathrm{Re}((EI)_G)$ and $\mathrm{Im}((EI)_L) = -\mathrm{Im}((EI)_G)$. Figure 8 shows such a condition for $R = 10\ \Omega$ and $f_{LC} = 4$ kHz.

It was shown above that there exists a Bragg's bandgap in the frequency range from 2.5 kHz to 6 kHz for the short circuit case [see Figs. 5(a) and 5(b)]. When inductors are introduced, a passband is induced by electromechanical resonance. For instance, for $R = 10\ \Omega$ and $f_{LC} = 4$ kHz a passband is induced near the resonant frequency in the Bragg's bandgap for the short circuit case, as shown in Fig. 9. Here the band structures are calculated based on both the Timoshenko beam model and by FEM since the electromechanical resonance leads to drastic changes of the effective material parameters (see Fig. 8). Although the result from using the Timoshenko beam theory indicates narrow bands of flexural wave, indicated by black arrows in Fig. 9(c), they are different from the results from FEM [51]. The main passbands calculated based on Timoshenko beam theory and by FEM agree, other than for very small frequency shifts.

The results indicate that the passbands induced by resonance cannot reach the Brillouin boundary. According to the band-CPAL correspondence, this predicts the existence of a periodic CPAL at the frequency associated with the maximum Bloch wavenumber, which is indicated by a red arrow in Fig. 9(c). Figure 10(a) provides the transmittance, that is also calculated using RRM when varying the cell number. Surprisingly, extremely high transmittance (CAPL) occurs periodically at the frequency associated with the maximum Bloch wavenumber at 3.956 kHz with the associated cell number N of {4, 12, 21, 29}. These are perfectly consistent with the prediction of Eq. (9) and Eq. (10) that, for example, gives for $\triangle N = 8$ or $\triangle N = 9$, $N_{\min} = 4$ at $\max\{qL\} = 0.8785\pi$. For $N_{\min} = 4$ and at 3.956 kHz, one of the eigenvalues of the two-by-two propagating flexural wave scattering matrix is $|s_1| \ll 1$ and the other is $|s_2| \gg 1$, shown in Fig. 10(b), which correspond, respectively, to absorber and laser as shown in Figs. 10(c) and 10(d) for the output to input energy ratio. Figures 10(e) and 10(f) provide the amplitudes, respectively, of the outgoing waves when the incident wave vectors are eigenvectors corresponding to s_1 and s_2.

V. CONCLUSIONS

We have investigated longitudinal and flexural wave propagation through periodically-structured $\mathcal{PT}$ symmetric elastic metamaterials both theoretically and numerically. For the beam, we calculated the results based on using the Euler and the Timoshenko beam theories, and compared them to the more accurate, but more expensive, plane stress FEM analysis and found that only when using the Timoshenko beam theory did we get significantly accurate results at high frequencies. We showed that the occurrence of apparently periodic CPALs with changing cell number in $\mathcal{PT}$ symmetric elastic metamaterials is an interference effect, and can directly be related to the band structure of the infinite periodic metamaterial. In particular, that the frequency, the minimum cell number and periodicity can be accurately predicted from examining the Bloch band, even for complex systems such as the proposed periodic $\mathcal{PT}$ symmetric piezoelectric metamaterial beam.

As expected, we show that the $\mathcal{PT}$ symmetric metamaterial beam can act as a multifunctional device at the CPAL frequency depending on the characteristics of the incident waves. In particular, it can function as an amplifier, absorber, laser or unidirectional output device, and has excellent performances in all these aspects according to our simulations. For instance, the significant amplifying effect of the 6-cell metamaterial gives rise to easily reached transmittance above 10. Although the existing developed piezoelectric structures with circuits can achieve many unusual functions for elastic wave control, such as nonreciprocity [52], rainbow trapping [53], and amplification [54], our proposed device has obvious advantages of comprehensive versatility and high performance. In addition, $\mathcal{PT}$ symmetry is a new mechanism for elastic wave control, and the $\mathcal{PT}$ symmetric arrangement is simple.

As such, our study and the associated analytical tools provide a new strategy for design of elastic wave devices. To this end, we demonstrate that a periodic CPAL can be induced in the Bragg's bandgap using the band-CPAL correspondence. The plausibility of this demonstration was aided by the ease in tunability of the effective properties of the proposed metamaterial through controlled shunt circuits. In addition, we developed an efficient high-frequency-accurate and time saving RRM based on the Timoshenko beam theory to calculate the scattering properties of periodic $\mathcal{PT}$ symmetric piezoelectric metamaterial beams. Due to the accuracy of this analysis in the needed high frequency range, it can be used in place of the much more expensive and time consuming FEM calculations. These contributions can potentially aid in the rapid development of designs with applications in signal processing.

ACKNOWLEDGMENTS

This research is supported by the National Natural Science Foundation of China under Grants No. 12172008 and No. 11991033.

APPENDIX: REVERBERATION-RAY MATRIX METHOD FOR CALCULATING TRANSMISSION AND REFLECTION

The reverberation-ray method [55] is used to calculate the scattering matrix of the structure due to numerical stability in transfer matrix methods at high frequencies. For this, the N-cell metamaterial beam is divided into n parts along the x direction and, thus, get $n + 1$ interfaces in the system. Dual coordinate systems, shown in Fig. 11, are used to describe the problem. For coordinate system $(Oxz)^{J(J+1)}$, considering the

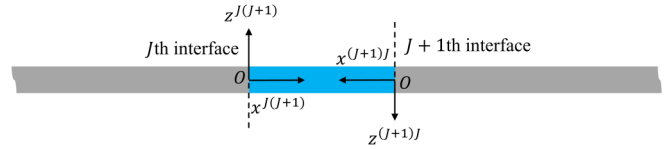

FIG. 11. The dual coordinates $(Oxz)^{J(J+1)}$ and $(Oxz)^{(J+1)J}$.

expression (17), the state vector $\mathbf{X}^{J(J+1)}$ can be written as

$$\mathbf{X}^{J(J+1)} = \mathbf{A}^{J(J+1)}\mathbf{a}^{J(J+1)} + \mathbf{D}^{J(J+1)}\mathbf{d}^{J(J+1)}, \tag{A1}$$

in which $\mathbf{A}^{J(J+1)}$ and $\mathbf{D}^{J(J+1)}$ have the same form as shown in Eq. (18), and

$$\mathbf{a}^{J(J+1)} = \left[a_1^{J(J+1)},\ a_2^{J(J+1)}\right]^T, \quad \mathbf{d}^{J(J+1)} = \left[d_1^{J(J+1)},\ d_2^{J(J+1)}\right]^T, \tag{A2}$$

represent, respectively, the arriving and departing wave amplitudes. As a result of the continuity condition at the interface,

$$\mathbf{X}^{J(J-1)}(0) = \mathbf{C}\mathbf{X}^{J(J+1)}(0), \quad \mathbf{C} = \begin{bmatrix} -1 & & & \\ & 1 & & \\ & & -1 & \\ & & & 1 \end{bmatrix}. \tag{A3}$$

The eight amplitudes in the two local coordinate systems $(Oxz)^{J(J+1)}$ and $(Oxz)^{J(J-1)}$ at the Jth interface can be expressed as

$$\mathbf{d}^J = \mathbf{S}^J\mathbf{a}^J, \tag{A4}$$

in which

$$\mathbf{S}^J = -[\mathbf{D}^J]^{-1}\mathbf{A}^J, \quad \mathbf{A}^J = [\mathbf{A}^{J(J-1)}, -\mathbf{C}\mathbf{A}^{J(J+1)}],$$
$$\mathbf{D}^J = [\mathbf{D}^{J(J-1)}, -\mathbf{C}\mathbf{D}^{J(J+1)}], \quad \mathbf{a}^J = [[\mathbf{a}^{J(J-1)}]^T, [\mathbf{a}^{J(J+1)}]^T]^T,$$
$$\mathbf{d}^J = [[\mathbf{d}^{J(J-1)}]^T, [\mathbf{d}^{J(J+1)}]^T]^T.$$

Furthermore, for the pair of dual coordinate systems shown in Fig. 11, there are the relations

$$W^{(J-1)J}(x^{(J-1)J}, \omega) = -W^{J(J-1)}(L^{(J-1)J} - x^{(J-1)J}, \omega), \tag{A5a}$$

$$\Theta^{(J-1)J}(x^{(J-1)J}, \omega) = \Theta^{J(J-1)}(L^{(J-1)J} - x^{(J-1)J}, \omega), \tag{A5b}$$

where $L^{(J-1)J}$ is the distance between the origin of the two coordinates. Equation (A5) leads to a relation for the phase of the amplitudes in each pair of dual coordinates given as

$$\mathbf{a}^{(J-1)J} = \mathbf{P}^{(J-1)J}\mathbf{d}^{J(J-1)},$$
$$\mathbf{P}^{(J-1)J} = \begin{bmatrix} -e^{-\lambda_1 L^{(J-1)J}} & 0 \\ 0 & -e^{-\lambda_2 L^{(J-1)J}} \end{bmatrix}.$$

Thus, at the Jth interface, there is the relation

$$\mathbf{a}^J = \mathbf{P}^J\bar{\mathbf{d}}^J, \tag{A6}$$

in which

$$\mathbf{P}^J = \begin{bmatrix} \mathbf{P}^{(J-1)J} & 0 \\ 0 & \mathbf{P}^{(J+1)J} \end{bmatrix}, \quad \bar{\mathbf{d}}^J = [[\mathbf{d}^{(J-1)J}]^T, [\mathbf{d}^{(J+1)J}]^T]^T,$$

where $\mathbf{P}^J$ is the local phase matrix.

Each continuity condition (A4) result in a relation between arriving wave amplitudes and departing wave amplitudes in each local coordinate. Thus, together they give

$$\begin{bmatrix} \mathbf{d}^1 \\ \mathbf{d}^2 \\ \vdots \\ \mathbf{d}^{N-1} \\ \mathbf{d}^N \end{bmatrix} = \begin{bmatrix} \mathbf{S}^1 & & & & \\ & \mathbf{S}^2 & & & \\ & & \ddots & & \\ & & & \mathbf{S}^{N-1} & \\ & & & & \mathbf{S}^N \end{bmatrix} \begin{bmatrix} \mathbf{a}^1 \\ \mathbf{a}^2 \\ \vdots \\ \mathbf{a}^{N-1} \\ \mathbf{a}^N \end{bmatrix}. \tag{A7}$$

According to Eq. (20), Eq. (A7) can be rewritten as

$$\begin{bmatrix} \mathbf{d_s} \\ \mathbf{d} \end{bmatrix} = \begin{bmatrix} \bar{\mathbf{S}}_{11} & \bar{\mathbf{S}}_{12} \\ \bar{\mathbf{S}}_{21} & \bar{\mathbf{S}}_{22} \end{bmatrix} \begin{bmatrix} \mathbf{a_s} \\ \mathbf{a} \end{bmatrix}, \tag{A8}$$

in which

$$\mathbf{d} = [[\mathbf{d}^{12}]^T, [\mathbf{d}^2]^T, \ldots, [\mathbf{d}^{N-1}]^T, [\mathbf{d}^{N(N-1)}]^T]^T,$$
$$\mathbf{a} = [[\mathbf{a}^{12}]^T, [\mathbf{a}^2]^T, \ldots, [\mathbf{a}^{N-1}]^T, [\mathbf{a}^{N(N-1)}]^T]^T.$$

Also, the local phase matrices (A6) lead to a global phase matrix $\mathbf{P}$ and the relation

$$\mathbf{a} = \mathbf{P}\mathbf{H}\mathbf{d}, \tag{A9}$$

where

$$\mathbf{P} = \begin{bmatrix} \mathbf{P}^{12} & & & & \\ & \mathbf{P}^2 & & & \\ & & \ddots & & \\ & & & \mathbf{P}^{N-1} & \\ & & & & \mathbf{P}^{N(N-1)} \end{bmatrix},$$

$$\mathbf{H} = \begin{bmatrix} \mathbf{L} & & & & \\ & \mathbf{L} & & & \\ & & \ddots & & \\ & & & \mathbf{L} & \\ & & & & \mathbf{L} \end{bmatrix}, \quad \mathbf{L} = \begin{bmatrix} 0 & 0 & 1 & 0 \\ 0 & 0 & 0 & 1 \\ 1 & 0 & 0 & 0 \\ 0 & 1 & 0 & 0 \end{bmatrix}.$$

Equations (A8) and (A9) combine to give

$$\mathbf{d_s} = \mathbf{S^r}\mathbf{a_s}, \tag{A10}$$

where

$$\mathbf{S^r} = \bar{\mathbf{S}}_{11} + \bar{\mathbf{S}}_{12}[(\mathbf{I} - \mathbf{P}\mathbf{H}\bar{\mathbf{S}}_{22})^{-1}\mathbf{P}\mathbf{H}\bar{\mathbf{S}}_{21}]. \tag{A11}$$

[1] M. I. Hussein, M. J. Leamy, and M. Ruzzene, Dynamics of phononic materials and structures: Historical origins, recent progress, and future outlook, Appl. Mech. Rev. **66**, 040802 (2014).

[2] Y.-F. Wang, Y.-Z. Wang, B. Wu, W. Chen, and Y.-S. Wang, Tunable and active phononic crystals and metamaterials, Appl. Mech. Rev. **72**, 040801 (2020).

[3] S. Bramhavar, C. Prada, A. A. Maznev, A. G. Every, T. B. Norris, and T. W. Murray, Negative refraction and focusing of elastic Lamb waves at an interface, Phys. Rev. B **83**, 014106 (2011).

[4] B. Deng, C. Mo, V. Tournat, K. Bertoldi, and J. R. Raney, Focusing and Mode Separation of Elastic Vector Solitons in a 2D Soft Mechanical Metamaterial, Phys. Rev. Lett. **123**, 024101 (2019).

[5] R. Xia, J. Yi, Z. Chen, and Z. Li, In situ steering of shear horizontal waves in a plate by a tunable electromechanical resonant elastic metasurface, J. Phys. D **53**, 095302 (2020).

[6] H. K. Zhang, Y. Chen, X. N. Liu, and G. K. Hu, An asymmetric elastic metamaterial model for elastic wave cloaking, J. Mech. Phys. Solids **135**, 103796 (2020).

[7] M. A. Attarzadeh, J. Callanan, and M. Nouh, Experimental Observation of Nonreciprocal Waves in a Resonant Metamaterial Beam, Phys. Rev. Appl. **13**, 021001(R) (2020).

[8] B. Li and K. T. Tan, Asymmetric wave transmission in a diatomic acoustic/elastic metamaterial, J. Appl. Phys. **120**, 075103 (2016).

[9] Y. Liu, Z. Liang, J. Zhu, L. Xia, O. Mondain-Monval, T. Brunet, A. Alù, and J. Li, Willis Metamaterial on a Structured Beam, Phys. Rev. X **9**, 011040 (2019).

[10] J. Yi, Z. Li, M. Negahban, R. Xia, and J. Zhu, Asymmetric viscoelastic metamaterials for broad bandgap design and unidirectional zero reflection, Mech. Syst. Signal Proc. **162**, 108101 (2022).

[11] X. Zhou, X. Liu, and G. Hu, Elastic metamaterials with local resonances: An overview, Theor. Appl. Mech. Lett. **2**, 041001 (2012).

[12] Y. Ashida, Z. Gong, and M. Ueda, Non-Hermitian physics, Adv. Phys. **69**, 249 (2020).

[13] V. V. Konotop, J. Yang, and D. A. Zezyulin, Nonlinear waves in PT-symmetric systems, Rev. Mod. Phys. **88**, 035002 (2016).

[14] R. El-Ganainy, K. G. Makris, M. Khajavikhan, Z. H. Musslimani, S. Rotter, and D. N. Christodoulides, Non-Hermitian physics and PT symmetry, Nat. Phys. **14**, 11 (2018).

[15] C. M. Bender and S. Boettcher, Real Spectra in Non-Hermitian Hamiltonians Having PT Symmetry, Phys. Rev. Lett. **80**, 5243 (1998).

[16] C. E. Rüter, K. G. Makris, R. El-Ganainy, D. N. Christodoulides, M. Segev, and D. Kip, Observation of parity–time symmetry in optics, Nat. Phys. **6**, 192 (2010).

[17] L. Feng, R. El-Ganainy, and L. Ge, Non-hermitian photonics based on parity–time symmetry, Nat. Photonics **11**, 752 (2017).

[18] X. Zhu, H. Ramezani, C. Shi, J. Zhu, and X. Zhang, PT-Symmetric Acoustics, Phys. Rev. X **4**, 031042 (2014).

[19] Y. Aurégan and V. Pagneux, PT-Symmetric Scattering in Flow Duct Acoustics, Phys. Rev. Lett. **118**, 174301 (2017).

[20] Z. Hou, H. Ni, and B. Assouar, PT-Symmetry for Elastic Negative Refraction, Phys. Rev. Appl. **10**, 044071 (2018).

[21] Z. Hou and B. Assouar, Tunable elastic parity-time symmetric structure based on the shunted piezoelectric materials, J. Appl. Phys. **123**, 085101 (2018).

[22] J. M. Lee, T. Kottos, and B. Shapiro, Macroscopic magnetic structures with balanced gain and loss, Phys. Rev. B **91**, 094416 (2015).

[23] J. Schindler, A. Li, M. C. Zheng, F. M. Ellis, and T. Kottos, Experimental study of active LRC circuits with PT symmetries, Phys. Rev. A **84**, 040101(R) (2011).

[24] C. Hang, G. Huang, and V. V. Konotop, PT Symmetry with a System of Three-Level Atoms, Phys. Rev. Lett. **110**, 083604 (2013).

[25] A. Mostafazadeh, Spectral Singularities of Complex Scattering Potentials and Infinite Reflection and Transmission Coefficients at Real Energies, Phys. Rev. Lett. **102**, 220402 (2009).

[26] Y. D. Chong, L. Ge, H. Cao, and A. D. Stone, Coherent Perfect Absorbers: Time-Reversed Lasers, Phys. Rev. Lett. **105**, 053901 (2010).

[27] Z. Lin, H. Ramezani, T. Eichelkraut, T. Kottos, H. Cao, and D. N. Christodoulides, Unidirectional Invisibility Induced by PT-Symmetric Periodic Structures, Phys. Rev. Lett. **106**, 213901 (2011).

[28] A. Regensburger, C. Bersch, M.-A. Miri, G. Onishchukov, D. N. Christodoulides, and U. Peschel, Parity–time synthetic photonic lattices, Nature (London) **488**, 167 (2012).

[29] L. Chang, X. Jiang, S. Hua, C. Yang, J. Wen, L. Jiang, G. Li, G. Wang, and M. Xiao, Parity–time symmetry and variable optical isolation in active–passive-coupled microresonators, Nat. Photonics **8**, 524 (2014).

[30] L. Shao, W. Mao, S. Maity, N. Sinclair, Y. Hu, L. Yang, and M. Lončar, Non-reciprocal transmission of microwave acoustic waves in nonlinear parity–time symmetric resonators, Nat. Electron. **3**, 267 (2020).

[31] Ş. K. Özdemir, S. Rotter, F. Nori, and L. Yang, Parity–time symmetry and exceptional points in photonics, Nat. Mater. **18**, 783 (2019).

[32] M.-A. Miri and A. Alù, Exceptional points in optics and photonics, Science **363**, eaar7709 (2019).

[33] J. Christensen, M. Willatzen, V. R. Velasco, and M.-H. Lu, Parity-Time Synthetic Phononic Media, Phys. Rev. Lett. **116**, 207601 (2016).

[34] Q. Wu, Y. Chen, and G. Huang, Asymmetric scattering of flexural waves in a parity-time symmetric metamaterial beam, J. Acoust. Soc. Am. **146**, 850 (2019).

[35] Matheus IN Rosa, M. Mazzotti, and M. Ruzzene, Exceptional points and enhanced sensitivity in PT-symmetric continuous elastic media, J. Mech. Phys. Solids **149**, 104325 (2021).

[36] M. Farhat, P.-Y. Chen, S. Guenneau, and Y. Wu, Self-dual singularity through lasing and antilasing in thin elastic plates, Phys. Rev. B **103**, 134101 (2021).

[37] J. Yi, M. Negahban, Z. Li, X. Su, and R. Xia, Conditionally extraordinary transmission in periodic parity-time symmetric phononic crystals, Int. J. Mech. Sci. **163**, 105134 (2019).

[38] S. Longhi, PT-symmetric laser absorber, Phys. Rev. A **82**, 031801(R) (2010).

[39] L. Ge, Y. D. Chong, and A. D. Stone, Conservation relations and anisotropic transmission resonances in one-dimensional PT-symmetric photonic heterostructures, Phys. Rev. A **85**, 023802 (2012).

[40] L. Ge, K. G. Makris, D. N. Christodoulides, and L. Feng, Scattering in PT- and RT-symmetric multimode waveguides: Generalized conservation laws and spontaneous symmetry breaking beyond one dimension, Phys. Rev. A **92**, 062135 (2015).

[41] V. Achilleos, Y. Aurégan, and V. Pagneux, Scattering by finite periodic PT-symmetric structures, Phys. Rev. Lett. **119**, 243904 (2017).

[42] I. S. Grudinin, H. Lee, O. Painter, and K. J. Vahala, Phonon Laser Action in a Tunable Two-Level System, Phys. Rev. Lett. **104**, 083901 (2010).

[43] C. M. Bender, D. C. Brody, and H. F. Jones, Complex Extension of Quantum Mechanics, Phys. Rev. Lett. **89**, 270401 (2002).

[44] D. W. L. Sprung, H. Wu, and J. Martorell, Scattering by a finite periodic potential, Am. J. Phys. **61**, 1118 (1993).

[45] D. J. Griffiths and C. A. Steinke, Waves in locally periodic media, Am. J. Phys. **69**, 137 (2001).

[46] From the piezoelectric materials database in software Comsol Multiphysics.

[47] N. W. Hagood and A. von Flotow, Damping of structural vibrations with piezoelectric materials and passive electrical networks, J. Sound Vib. **146**, 243 (1991).

[48] G. Wang, Analysis of bimorph piezoelectric beam energy harvesters using Timoshenko and Euler–Bernoulli beam theory, J. Intell. Mater. Syst. Struct. **24**, 226 (2013).

[49] C. M. Wang, J. N. Reddy, and K. H. Lee, *Shear Deformable Beams and Plates: Relationships with Classical Solutions* (Elsevier, Amsterdam, 2000).

[50] K. F. Graff, *Wave Motion in Elastic Solids* (Courier Corporation, New York, 2012).

[51] This is a non-Hermitian system with strong electromechanical resonance that leads to results from FEM with noise in the resonant frequency region. The eigenvalue solver SPOOLES in COMSOL is used, and the convergent results in Fig. 9(c) are obtained by refining the mesh using over 4 million degrees of freedom.

[52] Y. Chen, X. Li, C. Scheibner, V. Vitelli, and G. Huang, Realization of active metamaterials with odd micropolar elasticity, Nat. Commun. **12**, 5935 (2021).

[53] M. Alshaqaq, C. Sugino, and A. Erturk, Programmable Rainbow Trapping and Band-Gap Enhancement Via Spatial Group-Velocity Tailoring in Elastic Metamaterials, Phys. Rev. Appl. **17**, L021003 (2022).

[54] Y. Y. Chen, R. Zhu, M. V. Barnhart, and G. L. Huang, Enhanced flexural wave sensing by adaptive gradient-index metamaterials, Sci. Rep. **6**, 35048 (2016).

[55] Z. Ma, J. Chen, B. Li, Z. Li, and X. Su, Dispersion analysis of lamb waves in composite laminates based on reverberation-ray matrix method, Compos. Struct. **136**, 419 (2016).